Microscopy and Microanalysis (2022), **28**, 1207–1220
doi:10.1017/S1431927621012940

Microscopy AND Microanalysis

Original Article

Atom Probe Tomography Analysis of Mica

Chiara Cappelli[1]*, Alberto Pérez-Huerta[1,2], Sardar B. Alam[3] and Tanya Prozorov[3]

[1]Department of Geological Sciences, The University of Alabama, Tuscaloosa, AL 35487, USA; [2]Alabama Museum of Natural History, The University of Alabama, Tuscaloosa, AL 35487, USA and [3]Division of Materials Sciences and Engineering, Ames Laboratory, Ames, IA 50011, USA

Abstract

Laser-assisted atom probe tomography (APT) is a relatively new, powerful technique for sub-nanometric mineral and biomineral analysis. However, the laser-assisted APT analysis of highly anisotropic and chemically diverse minerals, such as phyllosilicates, may prove especially challenging due to the complex interaction between the crystal structure and the laser pulse upon applying a high electric field. Micas are a representative group of nonswelling clay minerals of relevance to a number of scientific and technological fields. In this study, a Mg-rich biotite was analyzed by APT to generate preliminary data on nonisotropic minerals and to investigate the effect of the crystallographic orientation on mica chemical composition and structure estimation. The difference in results obtained for specimens extracted from the (001) and (*hk*0) mica surfaces indicate the importance of both experimental parameters and the crystallography. Anisotropy of mica has a strong influence on the physicochemical properties of the mineral during field evaporation and the interpretation of APT data. The promising results obtained in the present study open the way to future innovative APT applications on mica and clay minerals and contribute to the general discussion on the challenges for the analysis of geomaterials by atom probe tomography.

Key words: 3D reconstructions, anisotropy, biotite, chemical composition, crystallographic orientation

(Received 26 February 2021; revised 5 September 2021; accepted 1 October 2021)

Introduction

Several techniques are routinely employed to observe and chemically characterize minerals at the micro- and nanometer scale. X-ray diffraction, scanning electron microscopy with energy-dispersive X-ray spectroscopy (SEM-EDS) and electron microprobe (EPMA) are useful for mineral bulk compositional estimates, whereas transmission electron microscopy (TEM) and high-resolution TEM (HRTEM) become methods of choice when investigating defects, interfaces, and atomic arrangements in confined spaces. More recently, atom probe tomography (APT), historically used for the analysis of conductive materials, has been successfully applied to study the chemical composition and the 3D structure of insulator minerals, thanks to the implementation of the laser-assisted field evaporation technique (Saxey et al., 2018). From the early applications of laser-assisted APT on minerals and biominerals (e.g., Gordon & Joester, 2011; McMurray et al., 2011; Arey et al., 2012; Gordon et al., 2012; Bachhav et al., 2013; Heck et al., 2014; Valley et al., 2015), APT is becoming a more widely used technique in geosciences (Reddy et al., 2020), including diverse fields such as biomineralogy (DeRocher et al., 2020; Pérez-Huerta et al., 2020) and planetary science (Daly et al., 2020; Lewis et al., 2020; Darling et al., 2021). Still, some fundamental aspects of APT application to minerals must be addressed to further improve the data quality. The nominal accuracy of chemical characterization by APT can diminish due to phenomena related to the mineral-laser interaction and resolution limitations of the technique. Isobaric interferences (i.e., overlap of species with the same mass-to-charge state ratio) (Larson et al., 2013*b*; La Fontaine et al., 2017; Reddy et al., 2020), ion pile-up, neutral molecules formation and molecular species dissociation (Saxey, 2011; Karahka & Kreuzer, 2013; Meisenkothen et al., 2015; Santhanagopalan et al., 2015; Pedrazzini et al., 2017; Peng et al., 2018), and preferential (direct current) or late ion evaporation between laser pulses (Bachhav et al., 2011; Saxey, 2011; Mancini et al., 2014) are examples of detrimental processes, which depend on the experimental parameters, yet are primarily related to the nature of the analyzed material. In the same way, spatial reconstructions of APT specimens may be affected by trajectory aberrations and atom migration (Larson et al., 2013*a*; Devaraj et al., 2017; Oberdorfer et al., 2018; De Geuser & Gault, 2020) that are strongly linked to the mineral crystallography and its chemical composition.

The relationship between crystallography, ion density distribution, and atom loss during the field evaporation process has been previously reported for semiconductors and insulators (Gault et al., 2010*b*; Diercks et al., 2013; Du et al., 2013; Morris et al., 2019; Cappelli & Pérez-Huerta, 2020). A recent study by Cappelli & Pérez-Huerta (2020) investigated the possible influence of the crystallographic orientation on the spatial reconstruction and the chemical composition estimate of standard isotropic minerals (spinel and galena), reporting negligible differences among the performed APT analysis. Yet, different results are expected for anisotropic minerals with higher compositional

*Corresponding author: Chiara Cappelli, E-mail: ccappelli@ua.edu

Cite this article: Cappelli C, Pérez-Huerta A, Alam SB, Prozorov T (2022) Atom Probe Tomography Analysis of Mica. *Microsc Microanal* **28**, 1207–1220. doi:10.1017/S1431927621012940

© The Author(s), 2021. Published by Cambridge University Press on behalf of the Microscopy Society of America. This is an Open Access article, distributed under the terms of the Creative Commons Attribution licence (https://creativecommons.org/licenses/by/4.0/), which permits unrestricted re-use, distribution, and reproduction in any medium, provided the original work is properly cited.

https://doi.org/10.1017/S1431927621012940 Published online by Cambridge University Press

and structural complexity, which are probably more representative of the natural diversity of the geological materials.

In this study, for the first time, a mica has been analyzed by APT with the main purpose of generating preliminary data showing how anisotropic minerals, such as phyllosilicates, can be characterized by this technique. Micas are nonswelling potassium clay minerals with a high negative charge (~0.9–1.0). These materials are of importance to petrological processes, for their ubiquity in metamorphic, sedimentary and igneous rocks, the variability in the chemical composition, and their ability to incorporate minor and trace elements (Yavuz, 2003; Ottolini et al., 2010). Considered petrogenic indicators, they provide information about magmatic processes such as partial melting or crystal fractionation (Fabre et al., 2002; Lepore et al., 2017). In addition to a characteristic layered crystal structure [tetrahedral–octahedral–tetrahedral (TOT) phyllosilicate type] (Fig. 1; e.g., Brigatti et al., 2006), the surface charge and the wide crystal size ranging from nanometers to meters, make micas suitable for numerous applications involving inorganic and organic molecules adsorption, and cation exchange (Pastré et al., 2010; Kan et al., 2015; Osuna et al., 2018; Hussein & Vegi, 2020; Pazos et al., 2020; Wu et al., 2020). Furthermore, micas have been employed in the production of nanocomposites, which make use of the optical and electrical properties of these minerals, for many industrial applications (e.g., microelectronic, insulators, aerospace industry) (Zhang et al., 2005; Krzesińska et al., 2006; Verbeek & Christopher, 2012; Zhao et al., 2019). The study of mica minerals at the atomic scale will improve understanding of the structural and chemical properties of these materials (e.g., defects, cation substitutions) and the molecular processes (e.g., adsorption) associated with them. Moreover, APT, with high spatial resolution (up to 0.15 and 0.06 nm for lateral and longitudinal, respectively; Larson et al., 2013*a*), overcomes some limitations of other conventional nanotechniques (e.g., nano-SIMS) for targeting analysis of phyllosilicate needed, for example, to study rare materials, such as chondrite serpentine (Daly et al., 2021).

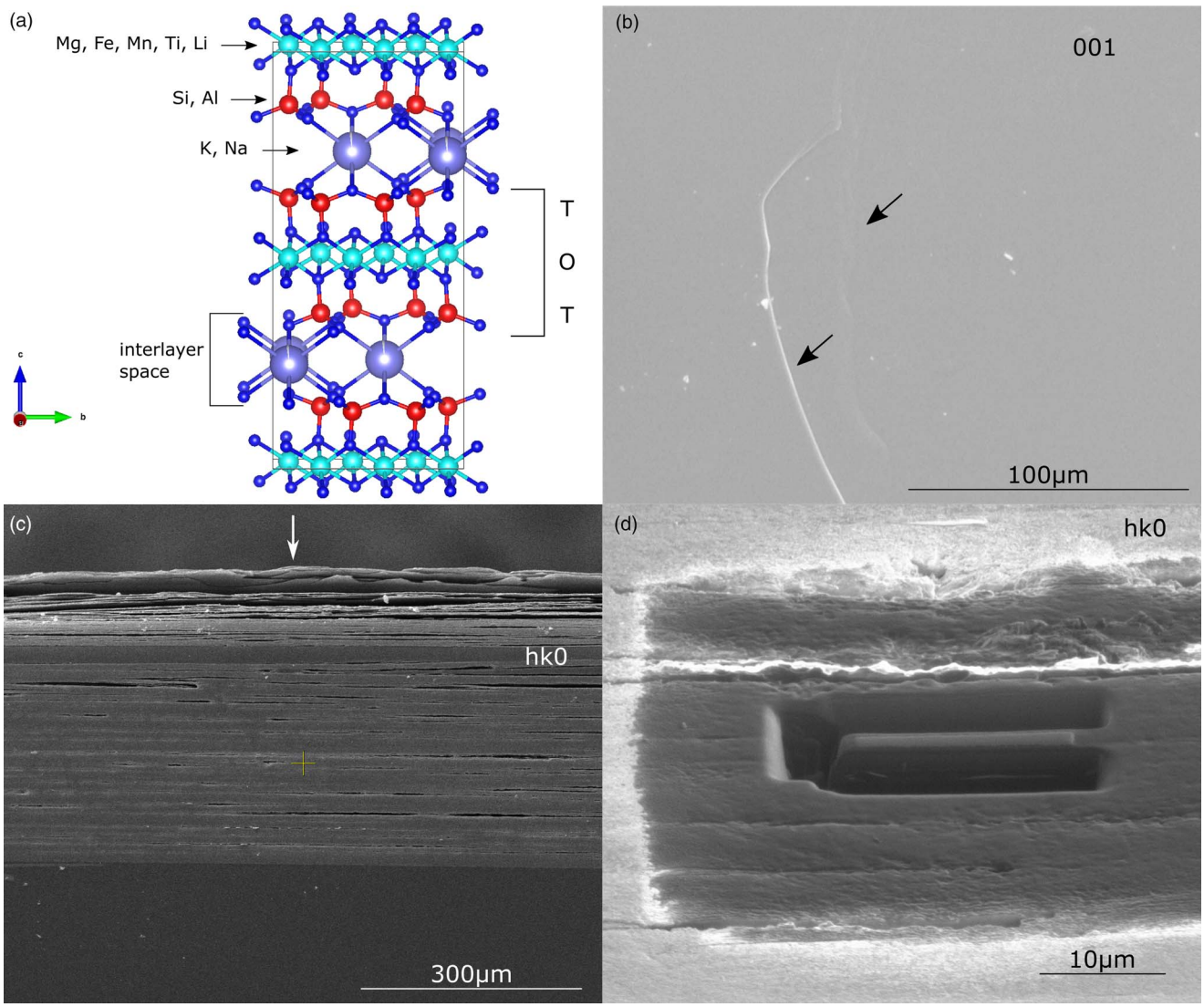

Fig. 1. (**a**) Simplified model of a mica structure showing the tetrahedral–octahedral–tetrahedral layer, the interlayer space and the typical cations occupying the different coordination position in the crystal lattice. SEM (**b,c**) and FIB (**d**) images of Mg-dominant biotite surface. (**b**) View of the (001) basal surface (black arrows indicate the edges of the mineral sheets). (**c,d**) View of the (*hk*0) surface where the layered structure is readily visible. White arrow in (**c**) indicates the exposed side of the sample undergoing delamination. In (**d**), wedge ready for lift-out.

https://doi.org/10.1017/S1431927621012940 Published online by Cambridge University Press

Material and Methods

Mineral Characterization

The mica used in this study was provided by the Alabama Museum of Natural History of the University of Alabama. The sample was analyzed by different techniques and compared to reference data for the correct interpretation of the APT results. A general structural formula was obtained by microprobe analysis [JEOL 8600 EPMA hosted at the Alabama Analytical Research Center (AARC)] and assuming all iron was ferrous:

$$K_{0.89}Na_{0.06}Mg_{1.59}Mn_{0.05}Fe_{1.16}Ti_{0.10}Al_{1.02}Si_{3.00}O_{10}(F, OH)_2.$$

Trace elements (Cr, Zn, Ni, Sr) were also identified while a percentage of fluorine was detected by EDS bulk analysis (JEOL 7000 FE SEM equipped with EDX hosted at the AARC) (see Supplementary Tables SI1 and SI2 for analysis details). According to the estimated chemical composition, the sample is a magnesium-rich biotite.

A biotite lamella was prepared and imaged utilizing scanning transmission electron microscopy in high-angle annular dark-field mode (HAADF-STEM) with an aberration-corrected Thermo Scientific Titan Themis Cubed hosted in the Sensitive Instrument Facility of the Ames Laboratory. The preparation of the sample is described in the Supplementary material. The TEM half grid with the prepared sample was loaded in a double-tilt holder, and images were recorded with the Cs-corrected probe with current of 20 pA at 200 kV. Before recording images, the biotite lamella was oriented on the zone-axis by parking the probe on the thickest region and recording and centering the Kikuchi band intersection visible in the Ronchigram. An expected value of 10 Å defining the d-spacing typical for biotite mica was determined (Fig. 2).

X-ray diffraction results are consistent with the sample characterization performed with the other techniques. Figure 3 shows a typical diffractogram of a biotite obtained by a Bruker D8 Discover XRD (hosted at the AARC) using a Co anode source with the average wavelength of 1.79 Å.

Sample Preparation for APT

Two different crystal orientations were considered, normal to [001] and [*hk*0] directions, respectively (Figs. 1b–1d). For the (001) basal surface specimens, a small mica flake (~1 × 1 cm and ~0.5 mm thick) was placed on a stub by gluing it with a carbon tape, the first few layers were peeled off by using regular adhesive tape, and the sample was coated with ~ 20 nm of gold to minimize surface charging effects during scanning microscopy (SEM) imaging and focus ion beam (FIB) milling. Due to the layered structure of mica (Fig. 1) and its easy delamination during manipulation, a sample flake (~1 × 1 cm and ~0.4 mm thick) was first placed in epoxy resin (001) surface-oriented, then the

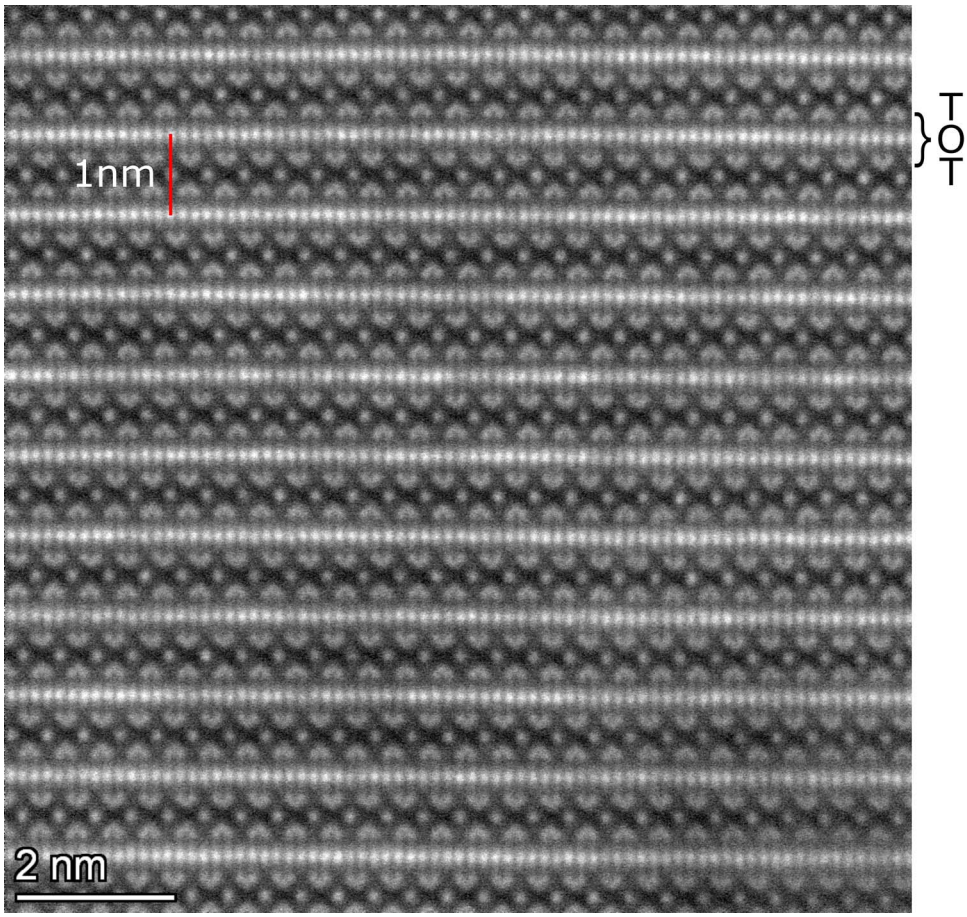

Fig. 2. High-angle annular dark-field scanning transmission electron microscopy (HAADF-STEM) image of (*hk*0) mica surface. A typical *d*-spacing of 10 Å (*c*-dimension) was measured and the tetrahedral–octahedral–tetrahedral (TOT) layers bound together by interlayer cations were revealed.

https://doi.org/10.1017/S1431927621012940 Published online by Cambridge University Press

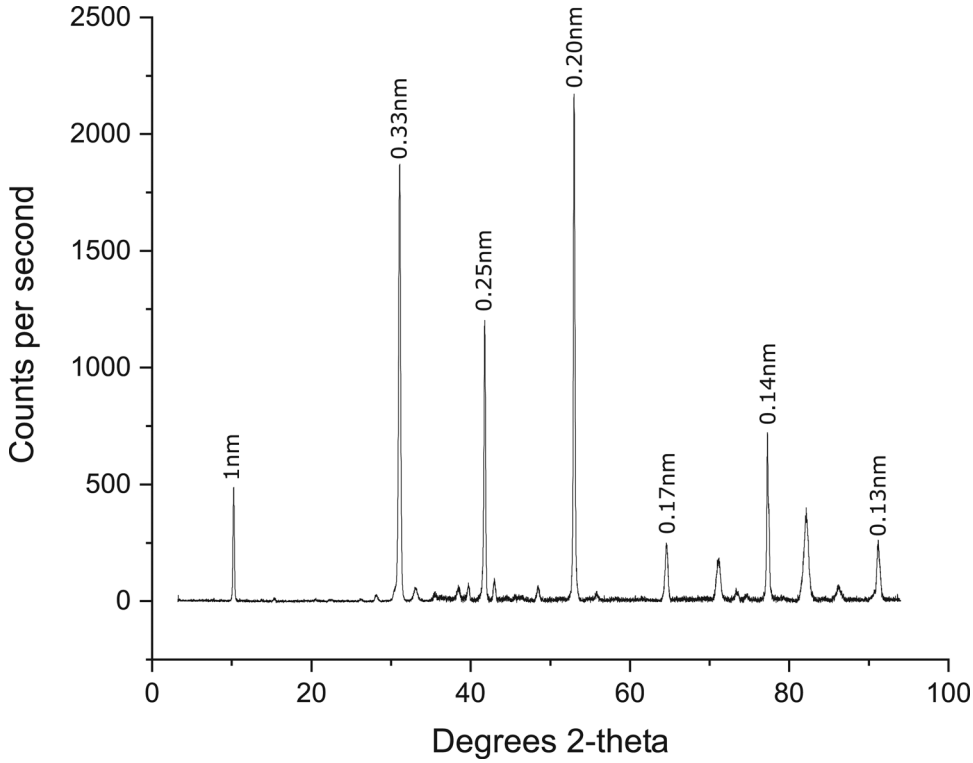

Fig. 3. Diffractogram of the mica sample showing the main reflections arisen from different pairs of layers of the mica crystallographic structure. Note the peak at 2θ–10.25° depicting the *c* lattice parameter dimension.

resin block was cross-cut by a diamond blade to expose the (*hk*0) surface. Finally, the sample was carefully polished by grinding paper, cleaned with MilliQ water and gold coated.

The needle-shaped specimens for APT were prepared following a conventional FIB protocol (Miller et al., 2007) using a dual-beam scanning electron microscope (Tescan Lyra FIB-FESEM or FEI Quanta 3D Dual Beam hosted at the AARC). Three specimens for each orientation were analyzed (total of six runs, Table 1). The radius of curvature and the shank angle ranged from 32 to 60 nm and 32° to 54°, respectively. For an overview of the different steps of the specimen preparation and the final tip shape, see Supplementary Figure SI1.

Local Electrode Atom Probe

In this study, a Local Electrode Atom Probe (LEAP) 5000 XS with a nominal flight path of 100 mm (housed at the AARC) was used in laser mode to analyze mica specimens. The laser pulse energy (PE) and the laser pulse rate (PR) were varied in the range 10–50 pJ and 100–200 kHz, respectively. In addition, a range of 0.2–0.3% for the detection rate (DR) was tested. Finally, the best parameter values were fixed and a total of six successful run were obtained (three for each crystallographic orientation) (Table 1). Since good resolution and low background were obtained, no further parameter's testing was performed, also taking into account that the increase of laser energy could lead to higher uneven tip heating [already observed for *hk*0 surface analysis (see the "Spatial reconstruction analysis" section in Results and Discussion)], higher detection to early fracture and higher pulse rates to larger thermal tails. Furthermore, it is worth noting that all the specimens extracted from the (001) surface suffered early fracture. This might be due to the specific layer's orientation normal to the analysis axes that in general decreases the analysis yield in layered materials (Kelly & Larson, 2012; Larson et al., 2013*b*).

The software IVAS 3.8.0 (Integrated Visualization and Analysis Software) from CAMECA was used for spectra creation and 2D and 3D reconstructions of the data sets. Individual spectrum peaks were associated with ion species consistent with the mineral bulk composition and the mass-to-charge state ratios.

Results and Discussion

APT Spectra and Chemical Composition

An APT spectrum of a representative mica specimen extracted from the (001) surface (Fig. 4a; Supplementary Fig. SI2) shows the characteristic peaks of the main species evaporated from the tip surface. Besides the structural cations already identified by EPMA, two minor elements appeared: lithium, whose peaks are associated with Li^+ isotopes with mass-to-charge state ratios 7 and 6 Da, and gallium (Ga^{++} and Ga^+ isotopes with mass-to-charge state ratios 34.5–35.5 and 69–71 Da, respectively). The presence of gallium was not unexpected and is ascribed to the use of the focused ion beam. Although Ga implantation during the milling process is minimized by the platinum sample screening, it is not always avoidable. Hence, Ga is not considered part of the mica structure but coming from an external source. Contrarily, lithium must undoubtedly be a structural cation, which was not detected by EPMA because of its low atomic mass. The determination of Li content in mica minerals has been a central issue in the past. Empirical relationships between Li_2O and SiO_2, Al_2O_3, MgO and other minor elements in mica

https://doi.org/10.1017/S1431927621012940 Published online by Cambridge University Press

Table 1. Instrument Settings and Input and Output Experimental Parameters.

Specimen/Data Set	biotite (001)			biotite (*hk*0)		
Reference	3981-M9	3979-M7	4160-M4	4411-M6	4408-M10	4410-M5
Instrument Model	LEAP 5000 XS					
Instrument settings						
Laser wavelength (λ)	355	355	355	355	355	355
Laser pulse energy (pJ)	20	50	50	20	30	50
Pulse frequency (kHz)	100	100	100	100	100	100
Evaporation control	Detection rate					
Detection rate (ions/pulse) %	0.3	0.3	0.3	0.3	0.3	0.3
Nominal flight path (mm)	100	100	100	100	100	100
Set point temperature (K)	30	30	30	30	30	30
Chamber pressure (Torr)	9.00×10^{-11}	4.40×10^{-11}	5.30×10^{-11}	1.50×10^{-10}	1.20×10^{-10}	1.40×10^{-10}
Data summary						
Analysis software	IVAS 3.8.0					
Total ions	6,375,239	2,625,777	3,808,088	12,425,310	23,390,600	10,525,872
Single (%)	72.6	73.1	64.1	64.5	66.5	63.8
Multiple (%)	26.3	25.6	34.9	33.9	32.1	34.7
Partial (%)	1.1	1.2	1	1.6	1.4	1.5
Reconstructed ions	5,482,225	2,315,870	337,8436	10,593,387	10,593,387	12,214,597
Ranged (%)	51	47	47	59	59	59
Mass calib. (peaks/interp.)	Lin. Method					
$(M/\Delta M)$ for $_{40}Mg^{++}$ /K^{+}	265	327	421	233	282	294
$(M/\Delta M_{10})^{c}$	83	123	159	98	116	124
Background (ppm/ns)	22.4	20.8	18.0	40.7	28.6	27.0
Reconstruction						
Final specimen state	Fractured	Fractured	Fractured	Good	Good	Good
Pre-/post-analysis imaging	SEM/na	SEM/na	SEM/na	SEM/SEM	SEM/SEM	SEM/SEM
Radius evolution model	Shank					
Field factor (k)	3.3	3.3	3.3	3.3	3.3	3.3
Image compression factor	1	1	1	0.9	0.9	0.9
Assumed E-field (V/nm)	18	18	18	18	18	18
Detector efficiency (%)	80	80	80	80	80	80
Avg. atomic volume (nm^3)	0.02	0.02	0.02	0.02	0.02	0.02
$V_{initial}$:V_{final} (V)	2,950:5,400	2,800:4,700	2,200:4,800	1,300:2,350	1,386:2,700	1,300:1,900

have been used to formulate regression equations enabling the estimation of lithium content from EPMA analysis (Tischendorf et al., 1997; Yavuz, 2001). Most recently, laser-induced breakdown spectroscopy (Fabre et al., 2002), laser ablation inductively coupled plasma mass spectroscopy (Breiter et al., 2017; Rosing-Schow et al., 2018), and SIMS (Ottolini et al., 2010) have been successfully applied for the identification of mica light and trace elements. APT not only provides the estimate of the concentration and isotopic ratios of those elements but, potentially, allows the assessment of their spatial distribution. In addition to Li, characteristic peaks of Ni^{+} (58 Da), Cu^{+} (63 Da), and Zn^{+} (64 Da) have been identified in mica spectra (Fig. 4).

In this study, numerous overlapping peaks were well resolved by the peak decomposition tool of the IVAS software on the basis of the isotopic ratios. Although, in some cases, the deconvolution was either very difficult or not viable. In fact, despite the high sensitivity of APT chemical analysis, the overlap of different element peaks is still an issue for the characterization of a mineral's composition by this technique (Reddy et al., 2020). For example, the estimate of Sr, previously detected in our sample by EPMA, was complicated by the overlap of its main peak at 44 Da (Sr^{2+}) with $^{28}Si^{16}O^{+}$ and the presence of a very low peak of $^{87}Sr^{2+}$ isotope at 43.5 Da from which the total element concentration was estimated. For a similar reason, Cr was not detectable

https://doi.org/10.1017/S1431927621012940 Published online by Cambridge University Press

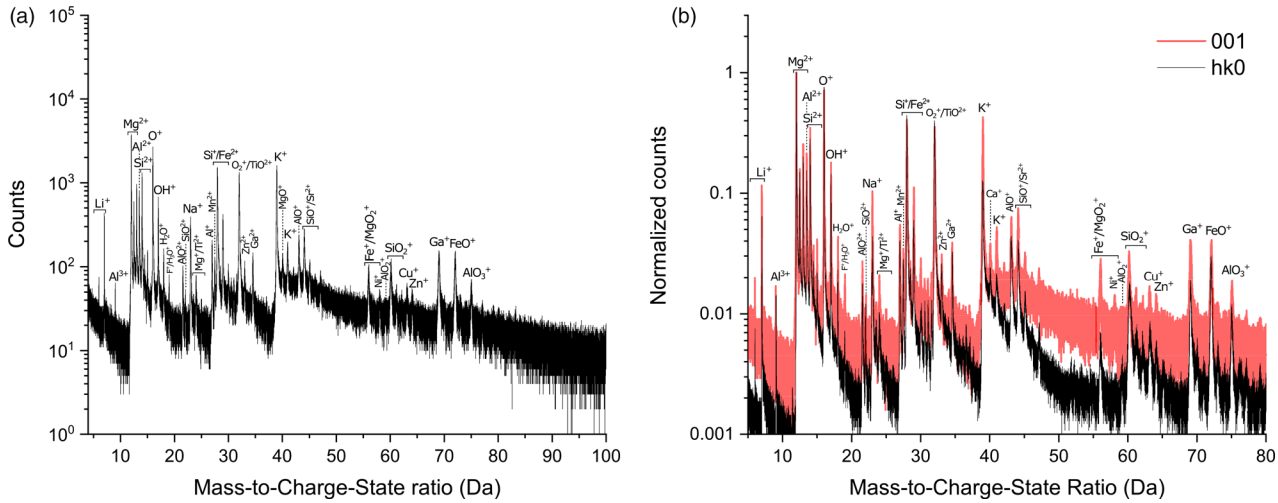

Fig. 4. Representative APT spectra of the studied Mg-biotite: (**a**) 001 specimen spectrum and (**b**) overlapped 001 and *hk*0 specimen spectra, normalized to the higher peak (i.e., $^{24}Mg^{2+}$ isotope).

by APT due to the overlapping of the main peaks with other elements and the very low concentration of this element leaving its nonoverlapping isotopes below the background. Likewise, the APT estimate of Ti concentration is not accurate because of the overlapping of almost all its main peaks [Ti^{2+} with Mg^{+} (24 Da); $^{48}Ti^{16}O^{2+}$ with O_2^{+} and Zn^{2+} (32 Da)]. In addition, while the deconvolution of Si^{+} and Fe^{2+} (28 Da) is quite reliable thanks to their isotope counts, it is difficult to discern between Fe^{+} and $^{24}Mg^{16}O_2^{+}$ (main peak 56 Da) whose isotopes are below the background level and hence almost or totally absent.

Despite these limitations, a general chemical composition was defined for the studied mica by APT for both the crystallographic orientations considered (Table 2). The first observation is the higher relative amount of Li, Na, and K cations and molecular species (e.g., SiO^{+}, AlO^{+}) obtained for the specimens extracted from the (001) surface with respect to (*hk*0) surface (001 and *hk*0 specimens hereinafter), as shown in Figure 4b where the normalized spectra of representative 001 and *hk*0 specimens were compared. Also, the total oxygen concentration is higher for the *hk*0 specimens, although always in deficit. The loss of oxygen during APT analysis has been already documented for several minerals in previous works (Gordon et al., 2012; Fougerouse et al., 2018; Saxey et al., 2018; Cappelli & Pérez-Huerta, 2020).

To simplify the assessment of the mineral stoichiometry, stoichiometric ratios (M/Si with M structural cation) for APT analysis and EPMA estimate were calculated (Table 3). Interestingly, the tetrahedral cations ratio (Al/Si) is near the stoichiometric value estimated by microprobe, for all the specimens analyzed by APT. To the contrary, interlayer cations, Na and K, are in excess for the 001 specimens and close to the stoichiometry ratio in the case of (*hk*0) surface. Mg appears always in excess. This behavior has been already observed during spinel and garnet APT characterization (Cappelli et al., 2021) and for Mg oxide at specific laser pulse energy conditions (Devaraj et al., 2013). This reveals a higher *apparent* APT efficiency in Mg detection or, conversely, the deficit of other structural elements of the mineral, which bias the estimate of the chemical composition. Different processes may have caused the observed element's deficit, including ion pile-up effect, neutral molecules formation or preferential evaporation (Saxey, 2011; Karahka & Kreuzer, 2013; Mancini et al., 2014; Meisenkothen et al., 2015; Peng et al., 2018). All these events may prevent atoms from being detected because they are either in the background or lost before they can even reach the detector, leading *de facto* to a decrease of the nominal atom detection efficiency.

Spatial Reconstruction Analysis

3D and 2D Plots

The spatial reconstruction of the mica tip-shaped specimens shows a nonuniform distribution of the main elements, especially for the 001 specimens (Fig. 5). At this orientation, the concentration of interlayer cations (K, Na) as well as that of molecular species (e.g., SiO, AlO, MgO) is much higher toward the center of the tip (Figs. 5a, 5b), whereas tetrahedral and octahedral cations are distributed along the edges of the specimen (Fig. 5c). Interestingly, the spatial distribution of Li follows the same pattern of the interlayer cations. Because the atom distribution appears to be consistent among the different identified ionic species, it is reasonable to infer that the encountered Li does not substitute octahedral cations, as one would expect for natural micas (Fig. 1a), but it is positioned in the interlayer (Fig. 5d). Otherwise, it is important to note that, similarly to K and Na, Li has a quite low evaporation field value. The low ionization energy of these cations could explain their similar behavior when a specimen is subjected to a high electric field and a laser pulse is applied. Additional experiments and analysis are needed in order to establish Li position in the crystal lattice of the studied mica.

The uneven distribution of ionic species along the tip-shaped specimen is related to the nonuniform electric field strength over the surface which, in turn, depends on the nature of the mineral and the sample crystallography (Yao et al., 2010; Morris et al., 2019). Specific areas of low ionic density (pole and lines zones) are revealed in 2D density plots of mica tetrahedral and octahedral cations (Fig. 6a). In general, the lower the ionic density, the higher the local electric field, and the lower the crystallographic plane order. The pole at the center of the tip apex (Fig. 6a) should, indeed, correspond to the ⟨001⟩ plane. It is also worth noting that the density variation through the tip length may also depend on the asymmetric distribution of the laser pulse (Müller et al., 2012).

To verify the existence of the electric field variability throughout the mica specimens, the charge state ratio (CSR) (M^{2+}/M^{+},

https://doi.org/10.1017/S1431927621012940 Published online by Cambridge University Press

Table 2. Elements Abundance Measured by APT for Each Mica Specimen and Crystallographic Orientation.

	001								
	3979			4160			3981		
	PE 50pJ-PR 100 kHz			*PE 50pJ-PR 100 kHz*			*PE 20pJ-PR 100 kHz*		
	Counts	Atomic %	Error %	Counts	Atomic %	Error %	Counts	Atomic %	Error %
Li	6,506	0.63	1.08×10^{-2}	9,927	0.68	9.47×10^{-3}	19,887	0.91	8.98×10^{-3}
Sr	829	0.08	4.13×10^{-2}	701	0.05	1.97×10^{-2}	1,496	0.07	3.08×10^{-2}
O	402,772	39.22	3.67×10^{-2}	599,723	41.14	3.06×10^{-2}	801,630	36.67	2.54×10^{-2}
F	961	0.09	6.61×10^{-3}	1,568	0.11	5.52×10^{-3}	3,353	0.15	6.21×10^{-3}
Na	16,065	1.56	1.91×10^{-2}	30,543	2.10	1.83×10^{-2}	35,188	1.61	1.16×10^{-2}
Mg	154,165	15.01	5.23×10^{-2}	220,141	15.10	4.49×10^{-2}	339,507	15.53	4.25×10^{-2}
Al	64,378	6.27	2.93×10^{-2}	81,519	5.59	2.48×10^{-2}	121,323	5.55	1.79×10^{-2}
Si	184,567	17.97	4.93×10^{-2}	209,756	14.39	1.53×10^{-1}	393,501	18.00	3.38×10^{-2}
K	102,781	10.01	4.03×10^{-2}	144,903	9.94	3.37×10^{-2}	263,896	12.07	3.24×10^{-2}
Ti	21,450	2.09	2.90×10^{-2}	24,883	1.71	2.51×10^{-2}	64,031	2.93	3.03×10^{-2}
Mn	4,410	0.43	1.02×10^{-2}	6,997	0.48	9.40×10^{-3}	9,684	0.44	7.61×10^{-3}
Fe	27,862	2.71	4.00×10^{-2}	87,054	5.97	1.59×10^{-1}	62,184	2.84	5.44×10^{-2}
Ni	1,790	0.17	1.27×10^{-2}	3,190	0.22	1.34×10^{-2}	4,480	0.20	1.41×10^{-2}
Cu	3,009	0.29	1.41×10^{-2}	3,821	0.26	1.13×10^{-2}	5,184	0.24	1.32×10^{-2}
Zn	5,691	0.55	2.65×10^{-2}	7,072	0.49	2.52×10^{-2}	11,808	0.54	2.90×10^{-2}
Ga	29,609	2.88	2.57×10^{-2}	26,037	1.79	1.82×10^{-2}	48,803	2.23	1.90×10^{-2}
	*hk*0								
	4410			4411			4408		
	PE 50pJ-PR 100 kHz			*PE 20pJ-PR 100 kHz*			*PE 30pJ-PR 100 kHz*		
	Counts	Atomic %	Error %	Counts	Atomic %	Error %	Counts	Atomic %	Error %
Li	19,055	0.33	3.61×10^{-3}	37,865	0.51	3.83×10^{-3}	65,715	0.52	3.01×10^{-3}
Sr	7,216	0.13	1.52×10^{-2}	6,288	0.08	6.84×10^{-3}	12,496	0.10	2.57×10^{-2}
O	2,650,038	46.42	1.71×10^{-2}	3,223,194	43.09	1.38×10^{-2}	5,743,196	45.70	1.12×10^{-2}
F	1,214	0.02	2.66×10^{-3}	3,095	0.04	2.18×10^{-3}	2,235	0.02	1.80×10^{-3}
Na	58,204	1.02	6.04×10^{-3}	80,428	1.08	5.25×10^{-3}	138,544	1.10	3.98×10^{-3}
Mg	849,382	14.88	2.12×10^{-2}	1,215,544	16.25	1.85×10^{-2}	1,855,288	14.76	1.40×10^{-2}
Al	347,506	6.09	1.27×10^{-2}	452,863	6.05	9.33×10^{-3}	759,169	6.04	8.24×10^{-3}
Si	799,689	14.01	9.08×10^{-3}	1,386,932	18.54	1.86×10^{-2}	2,117,022	16.85	6.01×10^{-2}
K	232,609	4.07	1.16×10^{-2}	489,851	6.55	1.20×10^{-2}	769,926	6.13	9.02×10^{-3}
Ti	132,269	2.32	6.86×10^{-3}	215,436	2.88	5.07×10^{-3}	252,211	2.01	4.01×10^{-3}
Mn	29,293	0.51	4.86×10^{-3}	3,7691	0.50	4.18×10^{-3}	60,612	0.48	3.22×10^{-3}
Fe	396,532	6.95	9.26×10^{-2}	143,391	1.92	6.47×10^{-3}	570,368	4.54	6.15×10^{-2}
Ni	3,803	0.07	3.72×10^{-3}	7,647	0.10	2.77×10^{-3}	12,210	0.10	3.44×10^{-3}
Cu	16,130	0.28	5.45×10^{-3}	22,169	0.30	5.08×10^{-3}	43,992	0.35	4.13×10^{-3}
Zn	31,825	0.56	1.76×10^{-2}	42,872	0.57	1.43×10^{-2}	87,037	0.69	1.16×10^{-2}
Ga	133,511	2.34	1.03×10^{-2}	115,361	1.54	7.75×10^{-3}	76,081	0.61	4.65×10^{-3}

https://doi.org/10.1017/S1431927621012940 Published online by Cambridge University Press

Table 3. Main Elements Stochiometric Ratios (M/Si) for EPMA and APT Mica Analysis.

		APT-001			APT-*hk*0		
	EPMA	R3979	R4160	R3981	R4410	R4411	R4408
Na	0.02	0.09	0.15	0.09	0.07	0.06	0.07
Mg	0.53	0.84	1.05	0.86	1.06	0.88	0.88
Al	0.34	0.35	0.39	0.31	0.43	0.33	0.36
Si	–	–	–	–	–	–	–
K	0.30	0.56	0.69	0.67	0.29	0.35	0.36
Ti	0.03	0.12	0.12	0.16	0.17	0.16	0.12
Mn	0.02	0.02	0.03	0.02	0.04	0.03	0.03
Fe	0.38	0.15	0.42	0.16	0.50	0.10	0.27

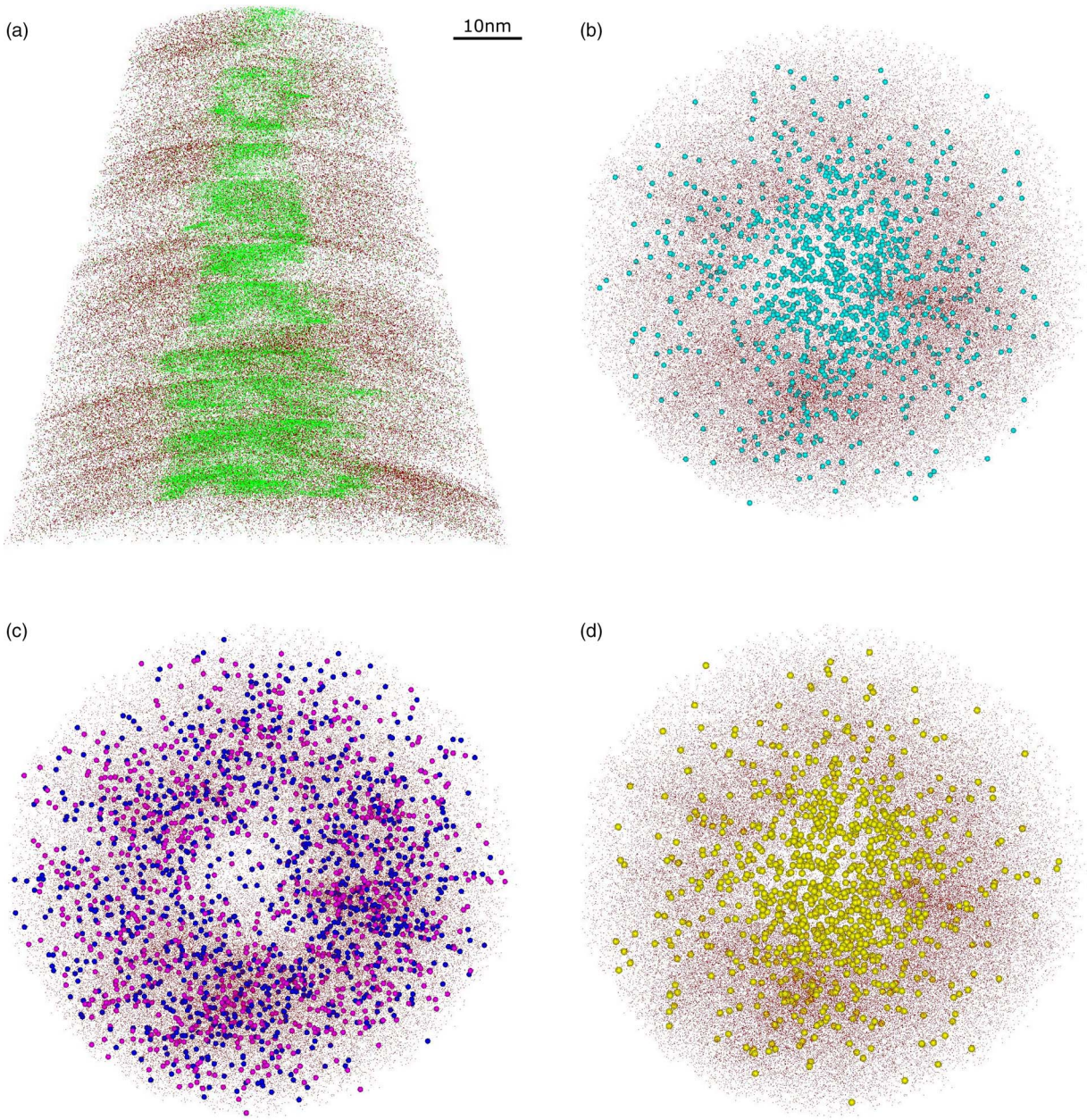

Fig. 5. 3D reconstructions of representative 001 specimen. Si atoms (dark red dots) are projected in the *z*–*x* plane (*x*-ortho projection) with **(a)** K (green dots) and in the *x*–*y* plane (*z*-ortho projection) with **(b)** MgO (light blue spheres), **(c)** Mg (dark blue spheres) and Al (pink spheres), and **(d)** Li (yellow spheres).

https://doi.org/10.1017/S1431927621012940 Published online by Cambridge University Press

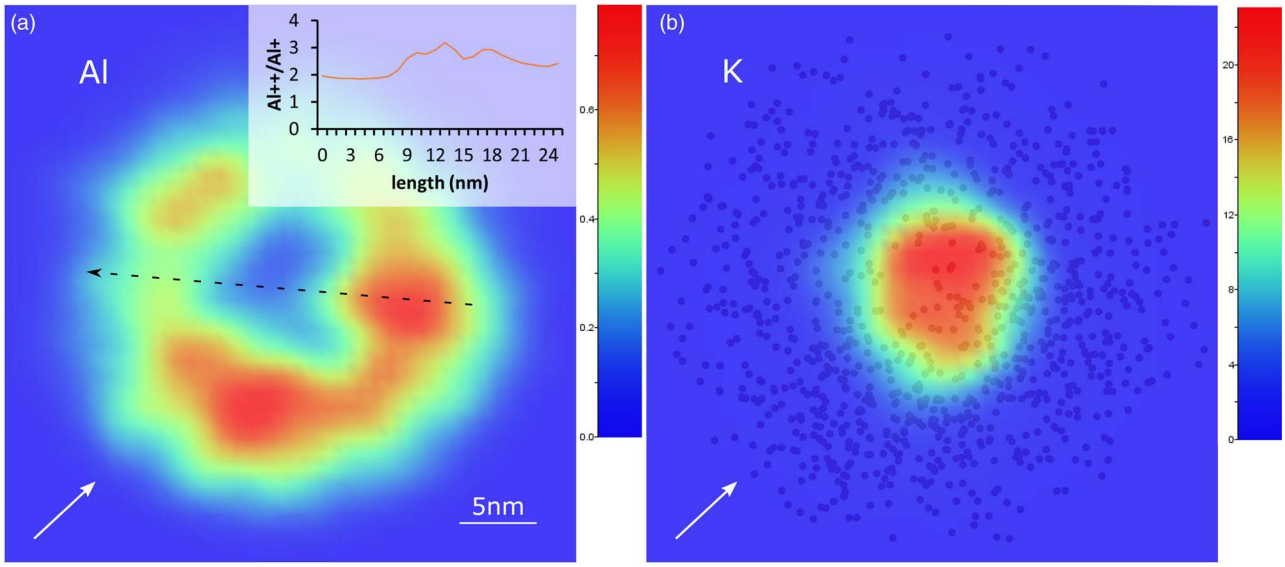

Fig. 6. 2D ion density plots (*z*-ortho projection) of a representative 001 specimen. (**a**) Al plot: the graph on the up-right shows the CSR measured along interlines, pole and line zones (black arrow) at a tip depth of 20 nm. (**b**) K plot: the spheres in the background are Si atoms. White arrows indicate the laser-beam direction.

with M = ionic species), that has previously proved to be a good surface field indicator (Mancini et al., 2014), was calculated over pole and line regions. Aluminum was taken as a representative element because it has clear peaks that are not affected by overlapping isotopes. The Al CSR value along a profile taken at a tip depth of 20 nm shows an increase from the inter-lines zone to a low-density line region with a maximum at the pole (inset in Fig. 6a). This supports the initial assumption regarding the local electric field distribution.

However, the density distribution of interlayer and molecular ionic species show an opposite pattern with respect to tetra and octahedral cations (Fig. 6b), consistent with the 3D reconstructions. This indicates that: first, the different bonding and coordination of the tetra/octahedral and interlayer cations affects the field evaporation; second, evaporation of molecular ionic species is favored at certain surface electric field conditions. High density at crystallographic poles has been previously reported for solutes in alloys (Oberdorfer et al., 2018) and is indicative of the fact that atom positions are somehow displaced after a field evaporation events, and that such a displacement depends on the crystallographic structure and chemistry of the mineral (Yao et al., 2015).

Previous studies demonstrated that APT reconstruction artifacts can arise from (1) the actual displacement of atoms throughout the surface and (2) the change in the local electric field direction that leads to trajectory aberrations. It has been proposed that, after the field evaporation of an atom, a *roll-up* effect prompts the migration of nearest-neighbors toward positions of lower coordination (i.e., higher field) by atomic relaxation (Gault et al., 2010*a*, 2012*a*; Oberdorfer et al., 2018). The prerequisite for this kind of mechanism is a preferential retention of the migrating atoms. In the case of mica, interlayer cations are subject to electrostatic forces and the nature of their bonding is predominantly ionic. In addition, K and Na as well as Li, as previously mentioned, have in theory very low evaporation field energies (Gault et al., 2012*b*). For these reasons, it is more probable that these cations undergo a preferential evaporation.

On the other hand, the layered nature of mica suggests that a change in the charge distribution must occur when the sheets of the TOT structure are progressively evaporated during APT analysis of 001 mica specimens. The charge density distribution of a surface atom depends on the electric field as well as the local chemistry (nearest neighbors). When an atom is removed from the surface, a rearrangement of the partial charges occurs and a change of the main electrostatic field direction can happen (Katnagallu et al., 2018; Klaes et al., 2021). Artifacts of registered atom positions would then derive from the change of the electric field configuration, leading to trajectory aberrations, and would reflect only an apparent atom's displacement. The configuration of the charge density of a material immersed in an electric field also redefines the bonding character between atoms (Loyola et al., 2016) and justifies the tendency of some elements to evaporate as molecular species for a certain value of the local field, as in the case of Mg, Fe, Al, and Si oxide species for mica. Likely, the bonds breaking of such molecules is energetically favored over the breaking of a single bond for the specific local charge density distribution.

Specimens extracted from the (*hk*0) surface showed a different ion spatial distribution and 2D density plot (Fig. 7), compared with 001 specimens. Interlayer and tetra/octahedral cations are more uniformly distributed (Fig. 7a), although a strong laser effect on the ion density distribution is apparent (Figs. 7b, 7c). High pulse energies may induce a nonuniform heating of the tip-shaped specimen, which promotes the appearance of a field strength gradient across the tip apex and eventually the formation of apex asymmetries (Müller et al., 2012). The alteration from an ideal spherical tip apex and, consequently, the variation of the local evaporation field, leads to apparent compositional anisotropy across the field of view, as the observed case of mica *hk*0 specimens.

The extent of Ga implantation along the specimen's edges during sample milling is also different for the 001 and *hk*0 specimens. Figure 8 shows a 3D reconstruction of representative tips, where isosurfaces are plotted to depict the boundaries between elements. Ga (in yellow) is distributed around the edge surface of the 001 specimens (Fig. 8a) while it follows the exposed edge side in *hk*0 specimens (Fig. 8b). The implantation of Ga during sample

https://doi.org/10.1017/S1431927621012940 Published online by Cambridge University Press

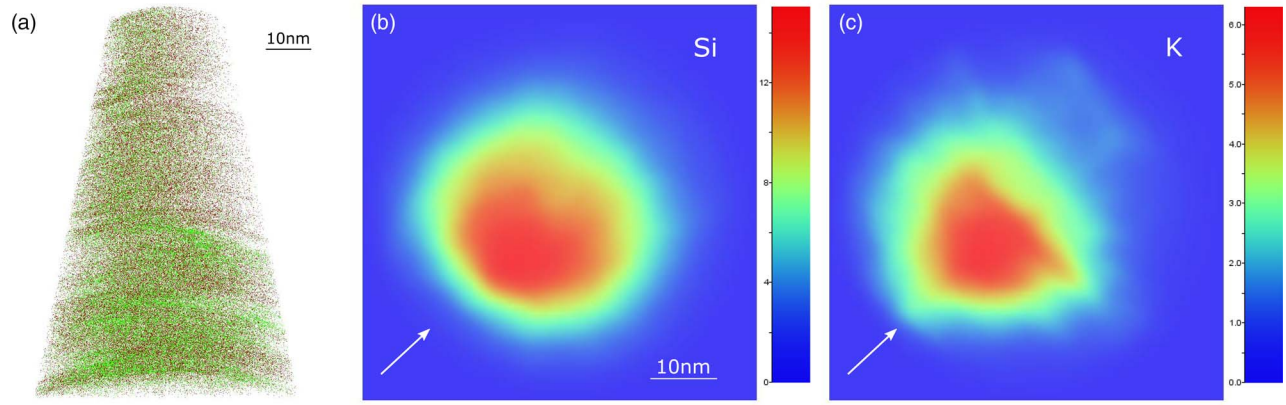

Fig. 7. 3D reconstruction (**a**) and 2D ion density plots (*z*-ortho projection) of Si (**b**) and K (**c**) of a representative *hk*0 specimen. In (**a**), Si atoms (dark red dots) are plotted (*x*-ortho projection) with K (green dots). White arrows indicate the laser-beam direction.

preparation is still an issue for APT analysis since it can cause damage and amorphization of the crystalline material and can promote fractures in brittle materials (Miller et al., 2007). Despite the minimization of this detrimental event, thanks to Pt protective deposition and low voltage specimen cleaning, mica seems particularly affected by Ga, likely due to its highly reactive edge surface where ions can be easily adsorbed.

Interestingly, the isosurfaces highlight a progressive variation of the mica platelets tilt in *hk*0 specimens (Fig. 8b). Apparently, the initial orientation is almost normal to the [*hk*0] direction and changes to a near to (001) surface-oriented platelet at ~120 nm tip depth.

Layered Structure and d*-Spacing*

The layered structure of mica is immediately apparent especially in the 001 specimen 3D reconstructions (Fig. 5a). Interlayer cations as well as tetrahedral and octahedral elements form series of layers that are sometimes interrupted by voids (Figs. 6a, 8a). This spatial distribution suggests that platelets of mica likely detach after a particular field evaporation event, breaking the

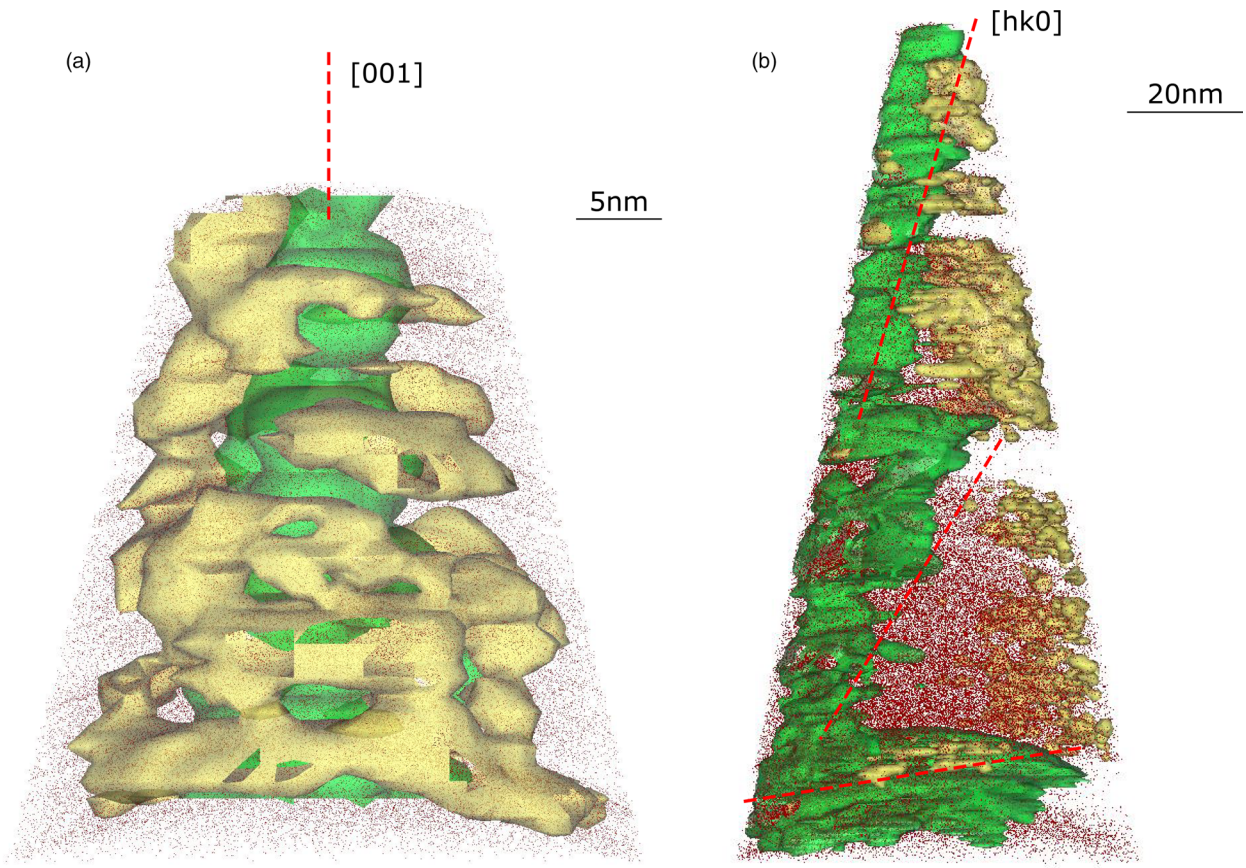

Fig. 8. 3D reconstructions of representative (**a**) 001 and (**b**) *hk*0 specimens. Si atoms (dark red dots) are plotted (*x*-ortho projection) with K (green) and Ga (yellow) isosurfaces. Red dashed lines indicate crystallographic orientation which for the *hk*0 specimen changes along the tip depth.

https://doi.org/10.1017/S1431927621012940 Published online by Cambridge University Press

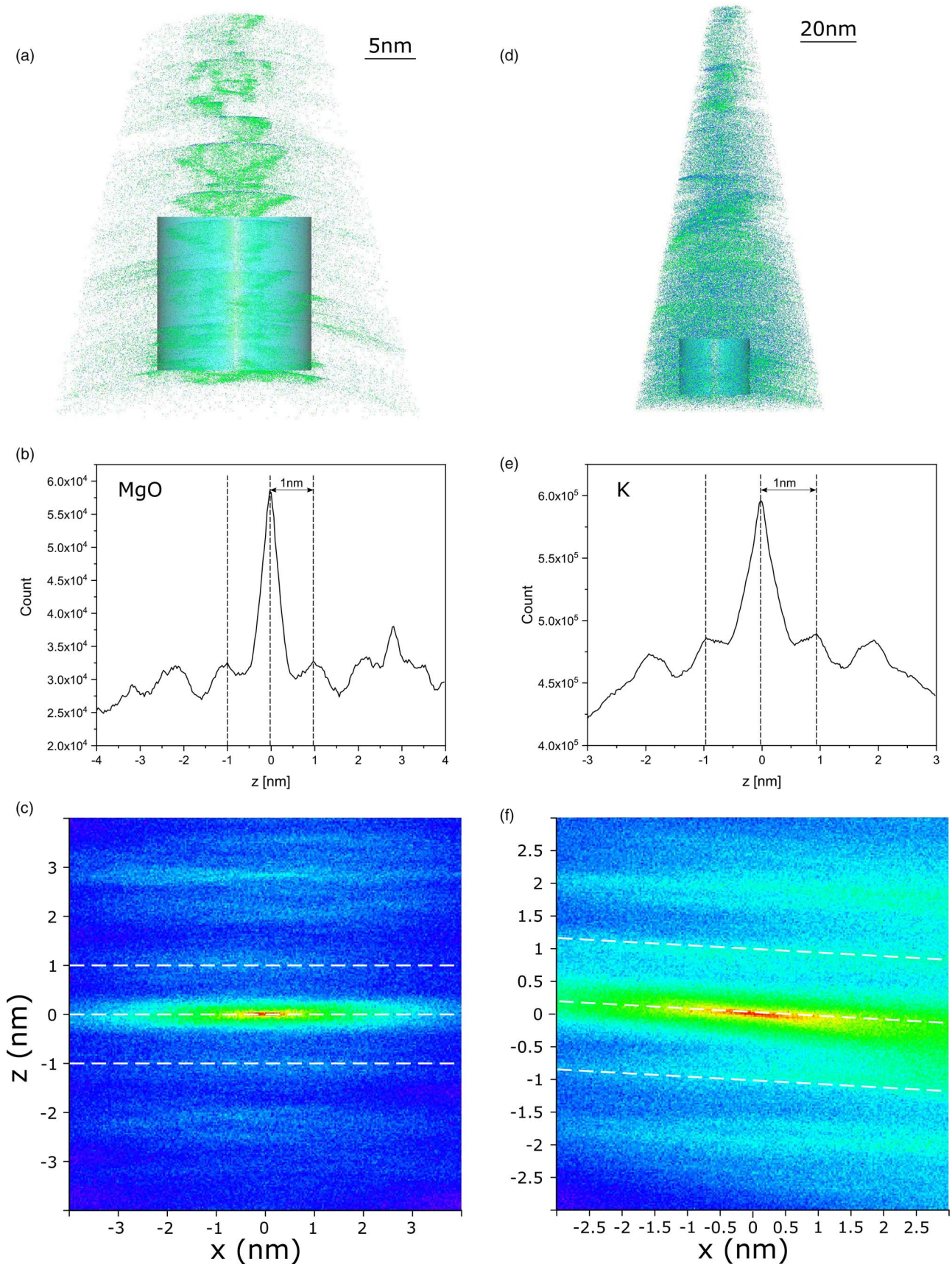

Fig. 9. 3D reconstructions (**a,d**) and spatial distribution maps (SDM) (**b,c,e,f**) of representative 001 and *hk*0 specimens. In (**a,d**), MgO (blue) and K atoms (green) are projected in the *z*–*x* plane (*x*-ortho projection); light blue cylinders are regions of interest where the SDMs were performed. In (**b,e**), intensity distribution of MgO and K, respectively, along the *z*-axis. In (**c,f**), view down the *y*-axis of the same data in (**b,e**), respectively. For the SDMs, the *z*-plane offset was 0 nm, and the cut in *xy* was 0.01 nm. Black and white dashed lines highlight the distance between atomic planes of the {001} family.

https://doi.org/10.1017/S1431927621012940 Published online by Cambridge University Press

continuity of the analysis (Fig. 8b). The discontinuous atom evaporation from the tip surface is well reflected in the voltage (direct current) curve from which the same reconstruction takes place (Supplementary Figs. SI3, SI4). In fact, laser tracking loss events occurred during some LEAP runs. It is unclear if the accommodation of mica platelets toward a (001) surface orientation occur during the tip preparation, or it was driven by the intrinsic discontinuity of the sample and the intense applied electric field during analysis.

The trajectory aberrations and poor continuity of the ion evaporation reduced the reconstruction resolution and prevented an accurate estimate of the mica *d*-spacing. However, a good approximation of the expecting *c* dimension value of 10 Å was measured by spatial distribution maps (SDM) (IVAS tool) for some regions of both 001 and *hk*0 specimens where several layers were depicted (Fig. 9). It is worth noting that the choice of the value of reconstruction parameters, namely the *k* field factor and the image compression factor (Lefebvre et al., 2016), is fundamental for the ion spatial distribution optimization and the knowledge of the crystallographic dimensions is useful in this regard.

Summary and Conclusion

Atom probe tomography is opening a new pathway for mineral investigation at the nanoscale level, enabling further insights in mineral structure and composition that will complement the knowledge gained by other techniques such as HRTEM or SIMS. In this study, APT was used, *for the first time*, to analyze a highly anisotropic mica mineral. Several observations were made that can be summarized as follows:

1. Both chemical and structural analysis of the studied Mg-rich biotite show significant differences between the two considered crystallographic orientation, highlighting the importance of the knowledge of the mineral physicochemical properties and their relationship with the mineral crystallography for the correct interpretation of the APT data set.
2. Apparent high-efficiency detection of Mg was observed regardless of the crystallographic orientation leading in all cases to biases in the mineral composition estimation. Also, an oxygen deficit was registered, especially for 001 specimens. Furthermore, peak overlap deconvolution was in some cases unattainable, hindering the correct concentration estimate of some elements. Still, stoichiometric ratios similar to those calculated by EPMA were obtained for Si, Al, Mn, Na, and K.
3. Ion spatial distributions show peculiar patterns that are artifacts of field evaporation. Displacements of atom positions in the reconstructions were probably due to trajectory aberrations arising from a rearrangement of the electric field after the first evaporation events (for 001 specimens) or a deviation of the tip apex from an ideal spherical geometry (for *hk*0 specimens).

Important questions remain to be answered about mica behavior subjected to an intense laser pulse under high electric field conditions, however the preliminary results obtained are extremely promising. Yet, some strategies could be employed for improving APT analysis of mica minerals. Analysis parameters not explored in the present study could be investigated. For example, higher temperatures could favor the analysis yield avoiding early fracture as it has been proved in the case of brittle materials. Furthermore, specimen preparation with a plasma focused ion beam (e.g., Xe^+ Plasma FIB-SEM dual-beam microscope) would avoid Ga implantation leading to a more representative reconstruction of the ion's spatial distribution.

Despite the limitations rising from the instrument technology (e.g., nominal efficiency, resolution) and issues related to the field evaporation process in nonconductive materials, basic investigation on both APT technology (e.g., terahertz-driven APT, Vella et al., 2021; new generation of APT detectors, Bacchi et al., 2021) and data processing [e.g., by new copyrighted (APT Suite 6 from CAMECA) and open source software (Kühbach et al., 2021)] is developing fast, providing analytical methods and atomic models needed to explain, predict, and correct the bias in mineral composition estimates and the inaccuracy in spatial reconstructions. Hence, future applications of APT for clay minerals are already in sight, with fundamental implications in geosciences, and other fields of study, including biosciences and materials sciences.

Supplementary material. To view supplementary material for this article, please visit https://doi.org/10.1017/S1431927621012940.

Acknowledgments. This research was funded by the U.S. National Science Foundation (NSF), grant numbers EAR-1647012 and EAR-2019870. T.P. and A.B.S. acknowledges support of Laboratory Directed Research and Development Program through Ames Laboratory. Microscopy work (FIB-SEM and STEM imaging) was performed using instruments in the Sensitive Instrument Facility at the Ames Laboratory, which is operated for the U.S. DOE by Iowa State University under contract # DE-AC02-07CH11358. Finally, this study utilized resources owned and maintained by the Alabama Analytical Research Center (AARC), supported by The University of Alabama.

References

Arey BW, Perera D, Kovarik L, Qafoku O, Felmy A & Gorman B (2012). Atom probe and TEM investigation of natural olivines. *Microsc Microanal* **18**(S2), 658–659.

Bacchi C, Da Costa G, Cadel E, Cuvilly F, Houard J, Vaudolon C, Normand A & Vurpillot F (2021). Development of an energy-sensitive detector for the atom probe tomography. *arXiv* preprint. arXiv:2103.04765.

Bachhav M, Danoix F, Hannoyer B, Bassat JM & Danoix R (2013). Investigation of O-18 enriched hematite (α-Fe_2O_3) by laser assisted atom probe tomography. *Int J Mass Spectrom* **335**, 57–60.

Bachhav M, Danoix R, Danoix F, Hannoyer B, Ogale S & Vurpillot F (2011). Investigation of wüstite ($Fe_{1-x}O$) by femtosecond laser assisted atom probe tomography. *Ultramicroscopy* **111**(6), 584–588.

Breiter K, Vaňková M, Galiová MV, Korbelová Z & Kanický V (2017). Lithium and trace-element concentrations in trioctahedral micas from granites of different geochemical types measured via laser ablation ICP-MS. *Mineral Mag* **81**(1), 15–33.

Brigatti MF, Galan E & Theng BKG (2006). Chapter 2. Structures and mineralogy of clay minerals. In *Developments in Clay Science*. Bergaya F, Theng BKG & Lagaly G (Eds.), vol. **1**, pp. 19–86. Elsevier.

Cappelli C & Pérez-Huerta A (2020). Effect of crystallographic orientation on atom probe tomography geochemical data? *Micron* **137**, 102910.

Cappelli C, Smart S, Stowell H & Pérez-Huerta A (2021). Exploring biases in atom probe tomography compositional analysis of minerals. *Geostand Geoanalytical Res* **45**(3), 457–476.

Daly L, Lee MR, Bagot P, Halpin J, Smith W, McFadzean S, O'Brien AC, Griffin S, Hallis LJ & Cohen BE (2020). Exploring Mars at the nanoscale: Applications of transmission electron microscopy and atom probe tomography in planetary exploration. *IOP Conf Ser: Mater Sci Eng* **891**, 012008.

Daly L, Lee MR, Darling JR, McCarrol I, Yang L, Cairney J, Forman LV, Bland PA, Benedix GK, Fougerouse D, Rickard WDA, Saxey DW, Reddy SM, Smith W & Bagot PAJ (2021). Developing atom probe tomography of phyllosilicates in preparation for extra-terrestrial sample return. *Geostand Geoanalytical Res* **45**, 427–441.

Darling JR, White LF, Kizovski T, Černok A, Moser DE, Tait KT, Dunlop J, Langelier B, Douglas JO, Zhao X, Franchi IA & Anand M (2021). The

shocking state of apatite and merrillite in shergottite Northwest Africa 5298 and extreme nanoscale chlorine isotope variability revealed by atom probe tomography. *Geochim Cosmochim Acta* **293**, 422–437.

De Geuser F & Gault B (2020). Metrology of small particles and solute clusters by atom probe tomography. *Acta Mater* **188**, 406–415.

DeRocher KA, Smeets PJM, Goodge BH, Zachman MJ, Balachandran PV, Stegbauer L, Cohen MJ, Gordon LM, Rondinelli JM, Kourkoutis LF & Joester D (2020). Chemical gradients in human enamel crystallites. *Nature* **583**(7814), 66–71.

Devaraj A, Colby R, Hess WP, Perea DE & Thevuthasan S (2013). Role of photoexcitation and field ionization in the measurement of accurate oxide stoichiometry by laser-assisted atom probe tomography. *J Phys Chem Lett* **4**(6), 993–998.

Devaraj A, Perea DE, Liu J, Gordon LM, Prosa TJ, Parikh P, Diercks DR, Meher S, Kolli RP, Meng YS & Thevuthasan S (2017). Three-dimensional nanoscale characterisation of materials by atom probe tomography. *Int Mater Rev* **63**(2), 68–101.

Diercks DR, Gorman BP, Kirchhofer R, Sanford N, Bertness K & Brubaker M (2013). Atom probe tomography evaporation behavior of C-axis GaN nanowires: Crystallographic, stoichiometric, and detection efficiency aspects. *J Appl Phys* **114**(18), 184903.

Du S, Burgess T, Tjing Loi S, Gault B, Gao Q, Bao P, Li L, Cui X, Kong Yeoh W, Hoe Tan H, Jagadish C, Ringer SP & Zheng R (2013). Full tip imaging in atom probe tomography. *Ultramicroscopy* **124**, 96–101.

Fabre C, Boiron M-C, Dubessy J, Chabiron A, Charoy B & Martin Crespo T (2002). Advances in lithium analysis in solids by means of laser-induced breakdown spectroscopy: An exploratory study. *Geochim Cosmochim Acta* **66**(8), 1401–1407.

Fougerouse D, Reddy SM, Saxey DW, Erickson TM, Kirkland CL, Rickard WDA, Seydoux-Guillaume AM, Clark C & Buick IS (2018). Nanoscale distribution of Pb in monazite revealed by atom probe microscopy. *Chem Geol* **479**, 251–258.

Gault B, La Fontaine A, Moody MP, Ringer SP & Marquis EA (2010*a*). Impact of laser pulsing on the reconstruction in an atom probe tomography. *Ultramicroscopy* **110**(9), 1215–1222.

Gault B, Moody MP, De Geuser F, La Fontaine A, Stephenson LT, Haley D & Ringer SP (2010*b*). Spatial resolution in atom probe tomography. *Microsc Microanal* **16**(1), 99–110.

Gault B, Danoix F, Hoummada K, Mangelinck D & Leitner H (2012*a*). Impact of directional walk on atom probe microanalysis. *Ultramicroscopy* **113**, 182–191.

Gault B, Moody MP, Cairney JM & Ringer SP (2012*b*). *Atom Probe Microscopy*. New York: Springer Science & Business Media.

Gordon LM & Joester D (2011). Nanoscale chemical tomography of buried organic–inorganic interfaces in the chiton tooth. *Nature* **469**(7329), 194–197.

Gordon LM, Tran L & Joester D (2012). Atom probe tomography of apatites and bone-type mineralized tissues. *ACS Nano* **6**(12), 10667–10675.

Heck PR, Stadermann FJ, Isheim D, Auciello O, Daulton TL, Davis AM, Elam JW, Floss C, Hiller J, Larson DJ, Lewis JB, Mane A, Pellin MJ, Savina MR, Seidman DN & Stephan T (2014). Atom-probe analyses of nanodiamonds from Allende. *Meteorit Planet Sci* **49**(3), 453–467.

Hussein IA & Vegi MR (2020). Defluoridation of drinking water using coalesced and un-coalesced mica. *Appl Water Sci* **10**(2), 64.

Kan Y, Tan Q, Wu G, Si W & Chen Y (2015). Study of DNA adsorption on mica surfaces using a surface force apparatus. *Sci Rep* **5**(1), 8442.

Karahka M & Kreuzer HJ (2013). Field evaporation of oxides: A theoretical study. *Ultramicroscopy* **132**, 54–59.

Katnagallu S, Dagan M, Parviainen S, Nematollahi A, Grabowski B, Bagot PAJ, Rolland N, Neugebauer J, Raabe D, Vurpillot F, Moody MP & Gault B (2018). Impact of local electrostatic field rearrangement on field ionization. *J Phys D: Appl Phys* **51**(10), 105601.

Kelly TF & Larson DJ (2012). Atom probe tomography 2012. *Ann Rev Mater Res* **42**(1), 1–31.

Klaes B, Lardé R, Delaroche F, Parviainen S, Rolland N, Katnagallu S, Gault B & Vurpillot F (2021). A model to predict image formation in the three-dimensional field ion microscope. *Comput Phys Commun* **260**, 107317.

Krzesińska M, Celzard A, Grzyb B & Marêché JF (2006). Elastic properties and electrical conductivity of mica/expanded graphite nanocomposites. *Mater Chem Phys* **97**(1), 173–181.

Kühbach M, Bajaj P, Zhao H, Çelik MH, Jägle EA & Gault B (2021). On strong-scaling and open-source tools for analyzing atom probe tomography data. *npj Comput Mater* **7**(1), 21.

La Fontaine A, Piazolo S, Trimby P, Yang L & Cairney JM (2017). Laser-assisted atom probe tomography of deformed minerals: A zircon case study. *Microsc Microanal* **23**(2), 404–413.

Larson DJ, Gault B, Geiser BP, De Geuser F & Vurpillot F (2013*a*). Atom probe tomography spatial reconstruction: Status and directions. *Curr Opin Solid State Mater Sci* **17**(5), 236–247.

Larson DJ, Prosa T, Ulfig RM, Geiser BP & Kelly TF (2013*b*). *Local Electrode Atom Probe Tomography*, p. 2. New York, USA: Springer Science.

Lefebvre W, Vurpillot F & Sauvage X (2016). *Atom Probe Tomography: Put Theory into Practice*. Academic Press.

Lepore GO, Bindi L, Pedrazzi G, Conticelli S & Bonazzi P (2017). Structural and chemical variations in phlogopite from lamproitic rocks of the Central Mediterranean region. *Lithos* **286–287**, 191–205.

Lewis JB, Floss C, Isheim D, Daulton TL, Seidman DN & Ogliore R (2020). Origins of meteoritic nanodiamonds investigated by coordinated atom-probe tomography and transmission electron microscopy studies. *Meteorit Planet Sci* **55**(6), 1382–1403.

Loyola C, Peralta J, Broderick SR & Rajan K (2016). Impact of extreme electrical fields on charge density distributions in Al_3Sc alloy. *J Vac Sci Technol A* **34**(6), 061404.

Mancini L, Amirifar N, Shinde D, Blum I, Gilbert M, Vella A, Vurpillot F, Lefebvre W, Lardé R, Talbot E, Pareige P, Portier X, Ziani A, Davesnne C, Durand C, Eymery J, Butté R, Carlin J-F, Grandjean N & Rigutti L (2014). Composition of wide bandgap semiconductor materials and nanostructures measured by atom probe tomography and its dependence on the surface electric field. *J Phys Chem C* **118**(41), 24136–24151.

McMurray S, Gorman B & Diercks D (2011). TEM and atom probe investigation of calcium carbonate precipitation in seawater. *Microsc Microanal* **17**(S2), 758–759.

Meisenkothen F, Steel EB, Prosa TJ, Henry KT & Prakash Kolli R (2015). Effects of detector dead-time on quantitative analyses involving boron and multi-hit detection events in atom probe tomography. *Ultramicroscopy* **159**, 101–111.

Miller MK, Russell KF, Thompson K, Alvis R & Larson DJ (2007). Review of atom probe FIB-based specimen preparation methods. *Microsc Microanal* **13**(6), 428–436.

Morris JHR, Cuduvally R, Melkonyan D, Zhao M, van der Heide P & Vandervorst W (2019). Atom probe of GaN/AlGaN heterostructures: The role of electric field, sample crystallography and laser excitation on quantification. *Ultramicroscopy* **206**, 112813.

Müller M, Smith GDW, Gault B & Grovenor CRM (2012). Compositional nonuniformities in pulsed laser atom probe tomography analysis of compound semiconductors. *J Appl Phys* **111**(6), 064908.

Oberdorfer C, Withrow T, Yu LJ, Fisher K, Marquis EA & Windl W (2018). Influence of surface relaxation on solute atoms positioning within atom probe tomography reconstructions. *Mater Charact* **146**, 324–335.

Osuna FJ, Cota A, Pavón E, Pazos MC & Alba MD (2018). Cesium adsorption isotherm on swelling high-charged micas from aqueous solutions: Effect of temperature. *Am Mineral* **103**(4), 623–628.

Ottolini LP, Schingaro E, Scordari F, Mesto E & Lacalamita M (2010). The role of SIMS in the investigation of the complex crystal chemistry of mica minerals. *IOP Conf Ser: Mater Sci Eng* **7**, 012023.

Pastré D, Hamon L, Sorel I, Le Cam E, Curmi PA & Piétrement O (2010). Specific DNA−protein interactions on mica investigated by atomic force microscopy. *Langmuir* **26**(4), 2618–2623.

Pazos MC, Bravo LR, Ramos SE, Osuna FJ, Pavón E & Alba MD (2020). Multiple pollutants removal by functionalized heterostructures based on Na-2-Mica. *Appl Clay Sci* **196**, 105749.

Pedrazzini S, London AJ, Gault B, Saxey D, Speller S, Grovenor CRM, Danaie M, Moody MP, Edmondson PD & Bagot PAJ (2017). Nanoscale stoichiometric analysis of a high-temperature superconductor by atom probe tomography. *Microsc Microanal* **23**(2), 414–424.

https://doi.org/10.1017/S1431927621012940 Published online by Cambridge University Press

Peng Z, Vurpillot F, Choi PP, Li Y, Raabe D & Gault B (2018). On the detection of multiple events in atom probe tomography. *Ultramicroscopy* **189**, 54–60.

Pérez-Huerta A, Walker SE & Cappelli C (2020). In situ geochemical analysis of organics in growth lines of antarctic scallop shells: Implications for sclerochronology. *Minerals* **10**(6), 529–542.

Reddy SM, Saxey DW, Rickard WDA, Fougerouse D, Montalvo SD, Verberne R & van Riessen A (2020). Atom probe tomography: Development and application to the geosciences. *Geostand Geoanalytical Res* **44**(1), 5–50.

Rosing-Schow N, Müller A & Friis H (2018). A comparison of the mica geochemistry of the pegmatite fields in southern Norway. *Canad Mineral* **56**(4), 463–488.

Santhanagopalan D, Schreiber DK, Perea DE, Martens RL, Janssen Y, Khalifah P & Meng YS (2015). Effects of laser energy and wavelength on the analysis of $LiFePO_4$ using laser assisted atom probe tomography. *Ultramicroscopy* **148**, 57–66.

Saxey DW (2011). Correlated ion analysis and the interpretation of atom probe mass spectra. *Ultramicroscopy* **111**(6), 473–479.

Saxey DW, Reddy SM, Fougerouse D & Rickard WDA (2018). The optimization of zircon analyses by laser-assisted atom probe microscopy. In *Microstructural Geochronology*, Mose DE, Corfu F, Darling JR, Reddy SM & Tait K (Eds.), pp. 293–313. American Geophysical Union.

Tischendorf G, Gottesmann B, Foerster H-J & Trumbull RB (1997). On Li-bearing micas: Estimating Li from electron microprobe analyses and an improved diagram for graphical representation. *Mineral Mag* **61**(6), 809–834.

Valley JW, Reinhard DA, Cavosie AJ, Ushikubo T, Lawrence DF, Larson DJ, Kelly TF, Snoeyenbos DR & Strickland A (2015). Nano- and micro-geochronology in Hadean and Archean zircons by atom-probe tomography and SIMS: New tools for old minerals. *Am Mineral* **100**(7), 1355–1377.

Vella A, Houard J, Arnoldi L, Tang M, Boudant M, Ayoub A, Normand A, Da Costa G & Hideur A (2021). High-resolution terahertz-driven atom probe tomography. *Sci Adv* **7**(7), eabd7259.

Verbeek J & Christopher M (2012). Mica-reinforced polymer composites. In *Polym Compos*, Thomas S, Kuruvilla J, Malhotra SK, Goda K & Sreekala MS (Eds.), pp. 673–713. EWiley–VCH Verlag GmbH & Co. KGaA.

Wu H, Lin S, Cheng X, Chen J, Ji Y, Xu D & Kang M (2020). Comparative study of strontium adsorption on muscovite, biotite and phlogopite. *J Environ Radioact* **225**, 106446.

Yao L, Gault B, Cairney JM & Ringer SP (2010). On the multiplicity of field evaporation events in atom probe: A new dimension to the analysis of mass spectra. *Philos Mag Lett* **90**(2), 121–129.

Yao L, Withrow T, Restrepo OD, Windl W & Marquis EA (2015). Effects of the local structure dependence of evaporation fields on field evaporation behavior. *Appl Phys Lett* **107**(24), 241602.

Yavuz F (2001). LIMICA: A program for estimating Li from electron-microprobe mica analyses and classifying trioctahedral micas in terms of composition and octahedral site occupancy. *Comput Geosci* **27**(2), 215–227.

Yavuz F (2003). Evaluating micas in petrologic and metallogenic aspect: I – Definitions and structure of the computer program MICA+. *Comput Geosci* **29**(10), 1203–1213.

Zhang Y-H, Dang Z-M, Xin JH, Daoud WA, Ji J-H, Liu Y, Fei B, Li Y, Wu J, Yang S & Li L-F (2005). Dielectric properties of polyimide-mica hybrid films. *Macromol Rapid Commun* **26**(18), 1473–1477.

Zhao W, Xu Y, Song C, Chen J & Liu X (2019). Polyimide/mica hybrid films with low coefficient of thermal expansion and low dielectric constant. *e-Polymers* **19**(1), 181–189.

https://doi.org/10.1017/S1431927621012940 Published online by Cambridge University Press